Computer Methods and Programs in Biomedicine 211 (2021) 106407

Contents lists available at ScienceDirect

Computer Methods and Programs in Biomedicine

journal homepage: www.elsevier.com/locate/cmpb

Optimal Spatial Sensor Design for Magnetic Tracking in a Myokinetic Control Interface

Marta Gherardini[a,b,*], Andrea Mannini[a,b,c], Christian Cipriani[a,b]

[a] The Biorobotics Institute Scuola Superiore Sant'Anna, 56127 Pisa, Italy
[b] Department of Excellence in Robotics and AI, Scuola Superiore Sant'Anna, 56127 Pisa, Italy
[c] IRCCS Fondazione Don Carlo Gnocchi, Firenze, Italy

ARTICLE INFO

Article history:
Received 10 December 2020
Accepted 3 September 2021

Keywords:
Magnetic sensors
Magnetic tracking
Myokinetic control interface
Sensor optimization
Prosthetic hand

ABSTRACT

Background and Objectives: Magnetic tracking involves the use of magnetic sensors to localize one or more magnetic objectives, in those applications in which a free line-of-sight between them and the operator is hampered. We applied this concept to prosthetic hands, which could be controlled by tracking permanent magnets implanted in the forearm muscles of amputees (the myokinetic control interface). Concerning the system design, the definition of a sensor distribution which maximizes the information, while minimizing the computational cost of localization, is still an open problem. We present a simple yet effective strategy to define an optimal sensor set for tracking multiple magnets, which we called the *Peaks* method.

Methods: We simulated a proximal amputation using a 3D CAD model of a human forearm, and the implantation of 11 magnets in the residual muscles. The *Peaks* method was applied to select a subset of sensors from an initial grid of 480 elements. The approach involves setting an appropriate threshold to select those sensors associated with the peaks in the magnetic flux density and its gradient distributions. Selected sensors were used to track the magnets during muscle contraction. For validating our strategy, an alternative method based on state-of-the-art solutions was implemented. We finally proposed a calibration phase to customize the sensor distribution on the specific patient's anatomy.

Results: 80 sensors were selected with the *Peaks* method, and 101 with the alternative one. A localization accuracy below 0.22 mm and 1.86° for position and orientation, respectively, was always achieved. Unlike alternative methods from the literature, neither iterative or analytical solution, nor a-priori knowledge on the magnet positions or trajectories were required, and yet the outcomes achieved with the two strategies proved statistically comparable. The calibration phase proved useful to adapt the sensors to the patient's stump and to increase the signal-to-noise ratio against intrinsic noise.

Conclusions: We demonstrated an efficient and general solution for solving the design optimization problem (i.e. identifying an optimal sensor set) and reducing the computational cost of localization. The optimal sensor distribution mirrors the field shape traced by the magnets on the sensing surface, being an intuitive and fast way of achieving the same results of more complex and application-specific methods. Several applications in the (bio)medical field involving magnetic tracking will benefit from the outcomes of this work.

1. Introduction

Magnetic tracking has recently drawn the attention of many researchers because of its potential applications in several fields, including medical procedures and biomedical equipment. Indeed, thanks to the transparency of the human body to low-frequency magnetic field [1], magnetic tracking has been devised for a number of intra-body applications in which a free line-of-sight between the operator and the end effector is hampered [2–6]. Generally speaking, in remote tracking a set of magnetic field sensors is used to retrieve the unknown *pose* (i.e., the position and orientation) of one or more magnetic markers, namely permanent magnets or transmitting coils. We recently proposed the use of magnetic tracking for controlling hand prostheses, by localizing permanent mag-

* Corresponding author at: Scuola Superiore Sant'Anna, Viale Rinaldo Piaggio, 34, 56025 Pontedera PI, Italy.
E-mail address: marta.gherardini@santannapisa.it (M. Gherardini).

https://doi.org/10.1016/j.cmpb.2021.106407

nets implanted into the forearm muscles through external sensors hosted in the socket [6]. Concerning the system design, while the benefit of using more sensors for improving the localization accuracy has been widely demonstrated [7–10], the definition of an optimal spatial design for the sensing assembly remains an open problem.

Indeed, although different solutions have been proposed in the literature [8,9,11,12], all of them considered a single marker tracking system, most of them were limited to a 2D grid sensor layout [8,9,12] whereas others were designed for specific applications [11]. As an example, Talcoth and Rylander [9] exploited the Fisher Information Matrix (FIM) to iteratively select an optimal sensor subset from a planar grid. Considering a single transmitting coil, they investigated how the optimal design varied for different poses of the transmitter. This approach had limitations: to compute the FIM, the knowledge of the exact pose of the considered transmitter was needed. Furthermore, the selection problem was solved through an optimization procedure that required computing the determinant of the FIM, whose dimensions increase linearly with the number of magnetic objectives. This makes the approach poorly scalable for multi-objectives tracking systems. More recently, Maréchal et al. [11] proposed a different approach to optimize the magnetic localization of catheters used in ventriculostomy procedures. They derived an optimal sensor arrangement using genetic algorithms (GAs) which proved better than classical grid configurations when localizing a permanent magnet. The selection problem was solved by exploiting a-priori knowledge on the reference trajectory travelled by the magnet during such procedures, as it is quite similar across patients. However, GAs usually require to set multiple parameters (and possibly constraints), and this is not always trivial to address [13]. Here, we propose a different approach which only takes as input the magnetic flux density and its gradient to select an optimal sensor subset. We applied it to a 3D anatomical workspace with multiple magnets, and confirmed that it led to accurate localization without requiring a-priori knowledge on their positions or trajectories.

We proved in early works [14,15] that a correlation exists between the presence of peaks in the magnetic flux density distribution and the localization accuracy. Indeed, a simple visual inspection of the recorded field distribution could provide an intuitive and rough anticipation on the accuracy of the localization [14]. Here, we assessed the viability of a sensor selection strategy embracing such concept for a myokinetic prosthesis controller. We called it the *Peaks* method. Starting from the anatomical setup used in [15], we simulated a representative proximal amputation and the implantation of 11 magnets into an equal number of residual forearm muscles. 480 magnetic field sensors were arranged around the residual limb.

First, a single case study was conducted for comparison of the *Peaks* method with results from [9], considering only the magnet implanted in the flexor carpi ulnaris (FCU). The study allowed to assess the dependence of the selected sensor (namely, the active sensor) positions on the magnet pose. Then, the *Peaks* method was compared with an alternative strategy based on state-of-the-art approaches, which we called the *FIM-GA* method. Both methods considered all implanted magnets in their initial (rest) position. The former selected only those sensors corresponding to the peaks in the magnetic flux density and its spatial gradient. The latter combined and adapted the approaches from [9] and [11] to draw an optimal sensor subset, by using a multi-objective GA to minimize three FIM-based cost functions. Thus, we could exploit the ability of GAs to search a wide range of the solution space rapidly, while evaluating the selection based on the information content of each sensor. This was intuitively more in line with the concept behind the *Peaks* method, which analyses the sensor recordings, and thus allowed to perform a fairer comparison for validating our approach. Evidence of the comparability between the two methods emerged from the outcomes of this work, featured in the first place by the topological similarity of the derived active sensor distributions. Following the selection process, magnets were independently moved along discrete trajectories to simulate muscle contraction, accounting for both axial and radial deformations. The orientation of the moving magnet was also varied by applying tilting. Pose localization accuracies obtained with the two configurations (i.e. the two sets of active sensors) were compared. Accurate and comparable localizations were always achieved, with errors below 3% the total trajectory length and below 9% the applied tilting.

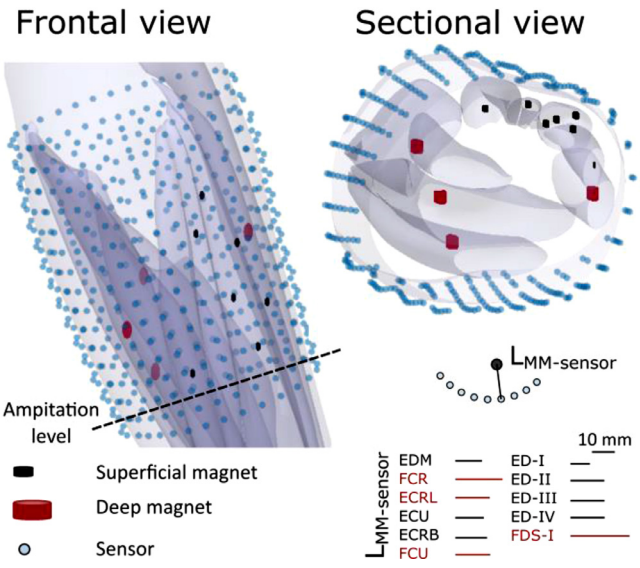

Fig. 1. Frontal view (upper left) and sectional view (upper right) of the implanted magnets and the sensor grid (blue dots, $N = 480$). $L_{MM-sensor}$ indicate the distance from a magnet to the nearest sensor (an example is schematically represented below the sectional view). Deeper magnets ($L_{MM-sensor} \geq 15\ mm$) are in red and have a radius and height equal to 2 mm. More superficial magnets are in black, and their dimensions are halved. Acronyms in Table I.

Finally, we extended the proposed method by introducing a calibration phase which sought to boost the customization of the active sensors according to a patient's specific anatomy. Simultaneous displacement of multiple extrinsic hand muscles was also implemented, mimicking the neural and mechanical connections coupling inter and intra-muscle contractions that exist in humans [16–21]. The accurate localization of magnets was confirmed, with a maximum error below 4% the trajectory length and below 9% the applied tilting. This study represents an important step forward towards the definition of an optimal sensing system design, not limited to myokinetic interfaces, but potentially useful for all magnetic tracking applications.

2. Materials and Methods

Aided by a 3D CAD model of a healthy human forearm, we simulated a representative proximal amputation (Fig. 1). Following the procedure described in [15], 11 magnets were arranged in the bellies of 11 forearm residual muscles, which we will refer to by using their acronyms, specified in Table I. A grid of 480 three-axes magnetic field sensors was arranged around the residual limb. The distance between adjacent sensors, indicated as $L_{inter-sensor}$, corresponded to a 12° angular step along the circumference and 10 mm distance along the axial direction.

It has been shown that a negative correlation exists between the localization accuracy and the distance between the magnets and the sensors, due to a reduced signal-to-noise ratio [7,8,10,11,14,22]. To address this aspect, we tuned the dimensions

Table I
Targeted muscles that received the implantation.

Acronyms	Muscles
EDM	Extensor digiti minimi
FCR	Flexor carpi radialis
ECRL	Extensor carpi radialis longus
ECU	Extensor carpi ulnaris
ECRB	Extensor carpi radialis brevis
FCU	Flexor carpi ulnaris
ED-I	Extensor digitorum – I compartment
ED-II	Extensor digitorum – II compartment
ED-III	Extensor digitorum – III compartment
ED-IV	Extensor digitorum – IV compartment
FDS-I	Flexor digitorum superficialis – I compartment

of the magnets based on their distance from their nearest sensor ($L_{MM-sensor}$). Specifically, magnets were modeled as Nd-Fe-B N45 grade cylindrical magnets (axial remanent magnetization Br = 1.27 T), with a 1 mm radius and height for more superficial magnets, and doubled dimensions for deeper ones (Fig. 1). We considered "deeper" all magnets having a $L_{MM-sensor}$ above or equal to 15 mm, so that the saturation limit of typical commercial magnetometers (LIS3MDL, STMicroelectronics), with a full scale of ± 16 G, was not reached. Once the magnets were arranged in the muscles (implanted) and their dimensions tuned, muscle contraction was simulated by displacing them along predefined discrete trajectories, described in the next section.

2.1. Muscle Contraction Model

In early work [15] we considered a simplified muscle contraction model which captured axial deformations only. In fact, skeletal muscles operate as a near-constant volume system, thus muscle shortening during contraction is transversely linked to radial deformation [23]. A technique called tensiomyography was developed in the recent years to measure radial displacement of muscles, by exploiting a high-precision digital displacement sensor applied to the muscle belly [24]. Parameters extracted from typical displacement curves indicate a peak radial displacement (i.e. an absolute spatial transverse deformation) in the order of half a centimeter [24]. Accordingly, we simulated muscle contraction by considering both an axial (d_a) and a radial (d_r) displacement component. As in [15], the amount of displacement was tuned based on the magnets implantation site. Specifically, magnets implanted in the distal belly moved by a maximum amount equal to $d_{a_{max}} = 10$ mm and $d_{r_{max}} = 5$ mm, respectively. Magnets implanted in the proximal muscle section moved proportionally to their distance from the muscle origin. Thus, the following rules applied:

$$D_r(x) = \begin{cases} \dfrac{x}{L/2} D_{r-max}, & x < \dfrac{L}{2} \\ D_{r-max}, & x \geq \dfrac{L}{2} \end{cases} \quad (1)$$

$$D_a(x) = \begin{cases} \dfrac{x}{L/2} D_{a-max}, & x < \dfrac{L}{2} \\ D_{a-max}, & x \geq \dfrac{L}{2} \end{cases} \quad (2)$$

where x is a coordinate lying on the curve that runs along the longitudinal axis of the muscle, and L is the length of the muscle belly at rest (Fig. 2). As in [15], the length of the distal aponeurosis was assumed equal to $L/2$.

The orientation of the *k-th* magnet was encoded with a unit vector of the form $[a_k, b_k, c_k]$. In the magnet's rest position, the magnetic moment vector was set to point radially towards the nearest sensor, to maximize the sampled magnetic field. However, since variability in the orientation due to both manual implantation and muscle contraction can be expected, tilting of the magnet during contraction was implemented. Specifically, it was simulated by applying an alternate ± 0.5 factor on a randomly selected component of the orientation vector, and subsequently normalizing it (Fig. 2).

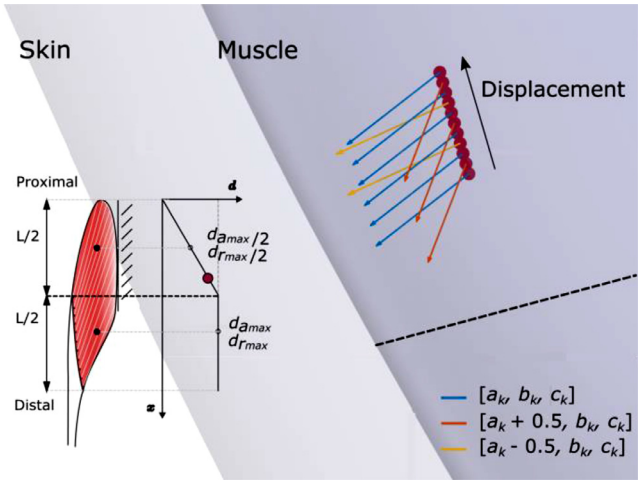

Fig. 2. Representative magnet trajectory. Red dots represent the magnet, whereas coloured arrows indicate the change in orientation due to the applied tilting. Since the magnet is implanted above the distal aponeurosis insertion (black dashed line), it moves proportionally to its distance from the muscle origin (see the inset on the left).

2.2. Sensing System Spatial Design

In the following, we describe the *Peaks* and the *FIM-GA* methods, implemented to determine an optimal sensing system design. Two different studies were performed. First, the *Peaks* method was applied to a single case study, to inspect how varying a single magnet pose affected the derived active sensor positions. Specifically, three conditions were tested for the single magnet implanted in FCU: (i) magnet in its original implantation site; (ii) tilting applied to the x component of the magnet orientation, by inverting the component sign; (iii) magnet radially moved 10 mm further from its nearest sensor. Then, the *Peaks* and the *FIM-GA* methods were used to select the active sensors when considering all magnets in their implantation sites. The obtained active sensors were subsequently used to collect the magnetic flux density while the targeted muscles underwent contraction. As in [15], we simulated the magnetic field generated by the magnets through the analytical model for a cylindrical magnet described and validated earlier [25,26]. All simulations were run in Matlab (MathWorks, Natick, MA) on a desktop computer with an Intel i7-6700 CPU running at 3.4 GHz, 32 GB of RAM and Windows 7.

1) Peaks method: with the magnet(s) in their rest position, the generated (compound) magnetic flux density was acquired on the entire sensor grid ($N = 480$ sensors). Random Gaussian noise with a standard deviation of 4 mG was added on the sampled signals, to mimic the characteristics of commercial magnetometers (LIS3MDL, STMicroelectronics). Then, following the procedure first introduced in [15], the 2D gradient (i.e. along the axial and the radial direction of the forearm) of the sampled magnetic flux density was computed (Fig. 3). Peaks locations on the initial sensor grid were identified by applying thresholding both to the magnetic flux density and its gradient distributions. Concretely, the threshold corresponded to the minimum amplitude difference allowed between an identified peak and its neighbors. Sensors associated with the aggregated peaks, i.e. with the compound peak locations identified

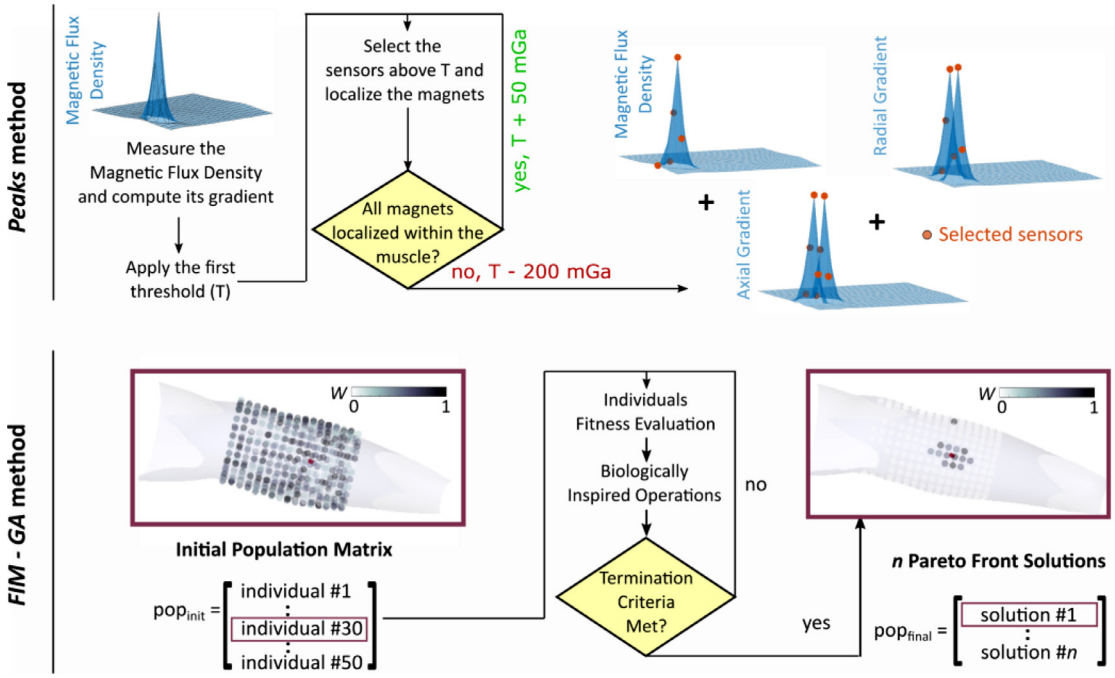

Fig. 3. *Peaks* method (upper panel) and *FIM-GA* method (lower panel) flow-charts for a single magnet. *Peaks* method: the first threshold value (T) is set, and the sensors associated with the peaks locations (identified through thresholding) are selected and used to localize the magnets. As long as localization is accurate, T is increased and the processed iterated, until at least one magnet is localized outside of its target muscle (critical T value). The final T is defined by lowering the reached critical value by 200 mG. *FIM-GA* method: the initial population matrix is defined. Each individual encodes the weights associated with the sensors of the grid (length equal to $N = 480$). An evolutionary process is applied to find the best individual. When termination criteria are met, the final solution is identified as the first row of the Pareto front matrix. Sensors having $w \geq 0.5$ are selected as active sensors.

in the field and in its gradients, were selected as active sensors and used to solve the localization problem (Fig. 3).

The threshold value was set empirically to ensure a trade-off between the number of selected sensors and the tracking accuracy. Such accuracy was evaluated by solving the localization problem (see next section) during muscle contraction, by considering all magnets and different active sensors derived using different threshold values. More precisely, starting from a threshold of 50 mG, the latter was incremented in steps of the same value until the localizer was no more able to retrieve the magnets poses (critical threshold value). Such critical value could be easily spotted when at least one of the magnets was localized outside of its workspace, i.e. outside of the corresponding targeted muscle belly. Indeed, we previously showed that, as long as magnets arrangement in space respects specific geometrical rules and the field spatial distribution is informative enough, then the localization of an indefinitely high number of magnets is accurate [14,15]. Here, magnets were arranged in the muscles through a *placing procedure* designed to fulfil such geometrical requirements. Thus, when the localization failed, it was most likely caused by a lack of information due to an oversampling of the measuring sites. When the critical threshold was reached, the search was stopped and its value was lowered by 200 mG to ensure a safety interval against noise. Indeed, the more the final threshold is set close to its critical value, the more the localization accuracy in presence of noise is likely to degrade, because the smoothing effect given by multiple acquisitions decreases [7,8,10,11,14,22].

2) *FIM-GA method:* GAs are a class of optimization algorithms inspired by the natural evolution [27]. They usually have one (or more) predefined goal in the form of a cost function, which the optimization process seeks to minimize. Candidate solutions are called individuals, which together form a population. Starting from an initial population, biologically inspired operations (namely selection, crossover and mutation) are iteratively applied to the individuals to derive an optimal solution, i.e. an individual with a lower value of the cost function [27]. Here, we considered the initial sensor grid as a nodes space where each node represented a possible sensor position. No geometrical constraint was imposed to the sensor arrangement, except for the physical distances imposed by the grid design. Individuals forming the population were numeric arrays with a length equal to the total number of nodes (i.e. $N = 480$). Each array element encoded the weight w of a specific sensor and could assume a continuous value between 0 and 1. The w values were iteratively updated by the algorithm until convergence, i.e. until an optimal weight array was found. At this point, only sensors associated with a $w \geq 0.5$ were selected as active sensors. The process was individually repeated for each magnet, and the active sensors selected for each magnet were finally gathered to form the final sensor grid.

A three-objective cost function was defined, which computed the FIM of the three magnetic flux density components (B_x, B_y, B_z). Let $p_k = [x_k, y_k, z_k, a_k, b_k, c_k]$ denote the vector of parameters describing the position and orientation of the *k-th* magnet in the Cartesian space. According to [9], the weighted FIM relative to B_x for the *k-th* magnet can be computed as:

$$FIM_{x,k} = \sum_{j=1}^{J} w_j \begin{pmatrix} \left(\frac{\delta B_{x_j}}{\delta x_k}\right)^2 & \cdots & \left(\frac{\delta B_{x_j}}{\delta x_k}\right)\left(\frac{\delta B_{x_j}}{\delta c_k}\right) \\ \vdots & \ddots & \vdots \\ \left(\frac{\delta B_{x_j}}{\delta c_k}\right)\left(\frac{\delta B_{x_j}}{\delta x_k}\right) & \cdots & \left(\frac{\delta B_{x_j}}{\delta c_k}\right)^2 \end{pmatrix} \quad (3)$$

where J is the number of sensors having $w_j \geq 0.5$. The same applies to B_y and B_z. Assuming that the noise terms in the sensor readings are independent, maximizing the FIM corresponds to minimizing the effect of noise on the parameters (p_k) estimation. This can be achieved by exploiting the D-optimality criterion [9] which involves computing the FIM determinant. Thus, for the *k-th* magnet, a solution was found by simultaneously minimizing

three (weighted) fitness functions defined as:

$$F_{x,k} = -\ln\left(\left|\sum_{j=1}^{J} w_j FIM_{j,x,k}\right|\right) \tag{4}$$

$$F_{y,k} = -\ln\left(\left|\sum_{j=1}^{J} w_j FIM_{j,y,k}\right|\right) \tag{5}$$

$$F_{z,k} = -\ln\left(\left|\sum_{j=1}^{J} w_j FIM_{j,z,k}\right|\right) \tag{6}$$

subject to:

$w_j \in [0.5,1]$, j=1, ..., J

$$\begin{cases} J - 10 \leq 0, & J > 10 \\ -(J-10) \leq 0, & otherwise \end{cases}$$

were $|\bullet|$ denotes the matrix determinant. FIMs were previously normalized by the total sum of the weights ($\sum_{i=1}^{N} w_i$), which allowed reducing weights for the non-selected sensors, while favoring higher weights for the selected ones. This was needed because many sensors would perform better than fewer sensors, as averaging would lower the noise effect. On the other hand, the imposed nonlinear constraint was needed to fix a (non-rigid) upper bound to the number of selected sensors. The bounding value was suggested by several studies searching for an optimal sensor number and spatial design that agree on the need of ~8-15 sensors per magnet [6,9,11,12,15,28].

The initial population matrix had 50 individuals on its rows, 39 of which were randomly initialized, one had all elements $w_i \geq 0.5$ (i.e. all sensors selected with random weights), whereas ten were defined through the *Peaks* method. To do this, the magnetic flux density generated by the *k-th* magnet on the whole sensor grid was simulated. Ten equally spaced thresholds in the interval [30, 300] mG were then used to select the active sensors corresponding to the peaks, as described above. For each considered threshold, one individual was encoded by assigning a random *w* in [0.5, 1] to all elements (sensors) corresponding to the detected peaks, while setting the others to zero. As previously shown in [11], building the initial population with a mix of random and optimized individuals effectively maximizes its diversity, which helps to avoid local minima.

The *gamultiobj* algorithm from the Matlab Optimization Toolbox was used to solve the optimization problem, and a trial-and-error (empiric) strategy was applied to select the best parameter set. As a result, we promoted mutation (with a rate of 0.08) instead of crossover (with a ratio of 0.1), and set the constraint tolerance to 1 in order to relax the upper-bound imposed to the sensor number. The maximum number of (stall) generations was set to (50) 250, while the default values were left unchanged for the other parameters. The algorithm finds the Pareto front of multiple cost functions, i.e. a set of individuals in the parameter space that have non-inferior cost function values [27]. As these individuals are equally good from the cost function perspective, after having verified that neither the number of sensors nor their distribution varied significantly across individuals (including the nearest individual to the Utopia solution [29]), we arbitrarily selected the one encoded in the first row of the final matrix to build the active sensor grid (Fig. 3).

2.3. Localization Problem

Once the two sets of active sensors were selected, the movement of the MMs along anatomically appropriate trajectories (described previously) was simulated. Similarly to [15], the displacement of the MMs was approximated by translating them, one at a time, along 11 equidistant checkpoints (0%, 10%, 20%, ..., and 100% the trajectory length). At each checkpoint, the simulated magnetic flux density was sampled on the two grids of active sensors and Gaussian noise was added. Sensor recordings at each checkpoint were stored and subsequently fed to a Matlab script that ran the Levenberg-Marquardt algorithm [30] to retrieve the poses of the MMs offline. The algorithm requires some user-defined initial conditions for the parameters to be estimated (i.e., the magnets poses). For the very first localization, the initial conditions were set by using the actual magnets orientation, while applying a random shift within 5 and 10 mm to their real spatial coordinates. Indeed, it is unknown how accurate the information about the magnets location following the implantation procedure would be. For the following localizations, the poses retrieved at the previous step were used as starting point for the algorithm search. Akin to several previous works [7,15,28], the algorithm approximated the MMs as point-like dipoles for solving the localization problem.

The localization errors, in terms of position and orientation, were assessed as:

$$E_p \approx e_{p,m} + e_{p,ct} \tag{7}$$

$$E_o \approx e_{o,m} + e_{o,ct} \tag{8}$$

where $e_{p,m}$ and $e_{o,m}$ account for inaccuracies in tracking the displacement of the moving magnet (i.e., model error), whereas $e_{p,ct}$ and $e_{o,ct}$ account for false predictions of simultaneous displacement affecting the non-moving magnets (i.e., crosstalk effect) [6]. Specifically, E_p and E_o respectively represent the difference between the actual and the estimated position and orientation displacement of the magnets, relatively to their rest poses.

2.4. Statistical Analysis

A statistical analysis was used to assess the comparability of the localization accuracy obtained with the active sensors selected with the *Peaks* and the *FIM-GA* method. To do this, the median values of $e_{p,m}$, $e_{p,ct}$, $e_{o,m}$ and $e_{p,ct}$ obtained for each magnet in each configuration were computed. The derived values were stored into eight separate vectors with a length equal to the number of magnets. The agreement of each paired measures (i.e. same error vector from the two configurations) was verified by deriving the Bland-Altman plot [31]. The latter is a statistical tool used to quantify the agreement between two quantitative measures. Practically, a 2D scatter plot is constructed in which the difference of the two paired measures is plotted against their mean value. The agreement between the two methods is established if at least 95% of the data points lie within $\pm$ 2 standard deviations of their mean difference (limits of agreement).

2.5. Calibration Phase and Muscles Co-Activation

Given the variability across patients, the customization of the sensor arrangement for a specific person could be obtained by providing information on the magnets trajectories to the sensors selection algorithm. Since such information is not available a-priori, we extended the proposed method by implementing a calibration phase which involved collecting the sensors recordings while the targeted muscles underwent contraction. Thus, a different set of active sensors could be identified in correspondence of each checkpoint along the magnets displacement, by applying the *Peaks* method. The active sensors selected at each checkpoint were finally gathered, and a compound active sensor grid was defined. In a real scenario, this could be achieved by performing multiple sensor acquisitions at a selected frequency while the subject is asked

to contract those muscles that received the implant. The threshold value set for the non-calibration case was used as starting point for the threshold setting procedure (the same described in section 2.2). Once the critical value was reached and the final threshold set, the active sensors were determined. The latter were subsequently used to sample the magnetic field during muscle contraction and localize the magnets offline, after that Gaussian noise was added.

Rather than moving one magnet per time, we assessed the feasibility of localizing multiple magnets during muscle co-activations, by simultaneously displacing multiple magnets along their entire trajectories. Our goal was to evaluate whether we could discriminate simultaneous muscle displacements, although without affecting the localization accuracy. First, we co-activated muscles acting on the wrist joint in an antagonist fashion, to mimic the biological way in which joint stabilization is achieved [18]. Thus, the co-contraction of ECU – FCU, and that of FCR - ECRL- ECRB, were implemented. Secondly, the simultaneous activation of ED-I - ED-II and that of ED-II - ED-IV were considered. This was done in consideration of several studies which proved a limited ability in humans to independently control distinct digital extensor compartments [19,21], with stronger influence given by adjacent digits compared to further ones [21]. EDM and FDS-I were treated as independent muscles, like in previous simulations. As multiple muscles (compartments) contracted together, no distinction was made between model and crosstalk errors for co-contraction simulations.

3. Results

3.1. Peaks *and* FIM-GA *Method*

Considering all implanted magnets, the critical threshold was identified when a value of 400 mG was reached, as the magnet in ED-IV was localized outside of the muscle volume. Thus, a final threshold of 200 mG was set for the magnetic flux density (and of 200 mG/$L_{inter-sensor}$ for the gradient, respectively), which was ∼50 times higher than the typical intrinsic noise of the sensor. Notably, tuning the magnets dimensions according to $L_{MM-sensor}$ allowed to select a higher threshold compared to the one used in [15] (equal to 5 mG), thus providing the system with a significantly increased robustness against noise.

First, results from the single case study are reported. The same threshold identified when considering all magnets was used for this study. The magnet implanted in FCU had a $L_{MM-sensor}$ of 15.3 mm. The active sensors selected with the *Peaks* method in such configuration formed a compact rectangular like shape around the nearest sensor (Fig. 4a). When tilting was applied on the x component of the orientation (inverted from - 0.71 to + 0.71), the active sensors distributed asymmetrically, forming a sort of arrow shape pointing towards the new magnet orientation vector (Fig. 5b). When the magnet was moved 10 mm further from the nearest sensor, the active sensors also moved further from it (Fig. 4c). For this latter case only, a halved threshold (100 mG) was used in order to gain a better visualization of the results, given the increased $L_{MM-sensor}$.

When the two selection strategies where applied by considering all implanted magnets, results revealed 80 active sensors selected through the *Peaks* method and 101 identified though the *FIM-GA* method. This corresponded to a reduction of ∼83% and ∼79% the initial grid, and to a sensor-to-magnet ratio of 7.3 and 9.2, respectively. The active sensors selected by the *Peaks* method generally clustered around the magnets rest position (Fig. 5). Active sensors appeared to be roughly normally distributed across the distal and central portion of the stump, which hosted the implanted magnets. A sparser sensor arrangement resulted from the application of the *GA* method. The active sensors distribution appeared slightly skewed, as few sensors were selected in the more proximal part of the stump (Fig. 5). Nevertheless, both strategies selected sensors mostly concentrated around the central portion of the stump (Fig. 5). Considering the computation time instead, notably the *Peaks* method could reach the final solution ∼15 times faster than the *FIM-GA* method.

Such similarity in the sensor distribution was seamlessly reflected in the achieved localization accuracy (Fig. 6). Indeed, the latter proved comparable in the two configurations both in terms of absolute localization error, and in terms of error distribution across different magnets (muscles). Concerning the position error, a maximum $e_{p,m}$ of 0.18 mm (0.17 mm) was obtained with the *Peaks* (*FIM-GA*) method, along with a maximum $e_{p,ct}$ of 0.22 mm (0.21 mm) (Fig. 6). Maximum $e_{p,m}$ values were obtained for the magnet implanted in FDS-I, whereas maximum $e_{p,ct}$ values were obtained for the magnet implanted in ED-II (Fig. 6). Overall, the total distances travelled by the magnets during contraction ranged between a minimum of 5.3 mm (ED-IV) to a maximum of 11.4 mm (ED-II and ED-III). The maximum position error associated with the shortest muscle displacement (ED-IV) in the two configurations, respectively equal to 0.17 mm and 0.16 mm, proved below 3% its entire trajectory length. In both configurations, the magnets implanted in ECRB, ED-II and FDS-I showed higher median errors compared to those implanted in the remaining muscles, both in terms of $e_{p,m}$ and $e_{p,ct}$ (Fig. 6).

The conclusions derived for the position error held true for the orientation error, as their trends closely matched (Fig. 6). The magnets implanted in ED-II showed the highest $e_{o,m}$, equal to 1.86° and 1.69° for the *Peaks* and *GA* method, respectively. Concerning the maximum $e_{o,ct}$, it proved equal to 1.80° in both cases and again for the magnet implanted in ED-II. Overall, the angular tilting applied to the magnets during contraction ranged between a minimum of 7.6° (FCR) to a maximum of 30° (FDS-I). The maximum orientation error associated with the minimum angular variation (FCR) in the two configurations, respectively equal to 0.62° and 0.49° mm, proved below 9% and 6% the applied tilting. Overall, the magnets implanted in ECRB, ED-II and FDS-I showed again higher median errors compared to the others, for both $e_{o,m}$ and $e_{o,ct}$ and in both configurations.

3.2. Statistical Analysis

As reported above, the localization accuracy obtained with the two selection methods proved overall comparable (Fig. 6). The agreement between the achieved results was confirmed by inspection of the derived Bland-Altman plots (Fig. 7). The resulting limits of agreement for position errors went from -0.02 mm to 0.03 mm, and from -0.01 mm to 0.01 mm for $e_{p,m}$ and $e_{p,ct}$, respectively. For the orientation errors, limits from -0.27° to 0.31° for $e_{o,m}$, and from -0.11° to 0.16° for $e_{o,ct}$ were obtained. Only one outlier was observed, showing 0.04 mm of difference in the two methods for $e_{p,m}$ (Fig. 7a).

3.3. Calibration Phase and Muscles Co-Activation

Given that the localization failed in correspondence of a threshold value of 800 mG (magnet in ED-IV mislocalized), a final threshold of 600 mG (and of 600 mG/$L_{inter-sensor}$ for the gradient) was set. The latter was ∼150 times higher than the typical sensor noise. A total of 86 active sensors were identified, resulting in a 7.8 sensor-to-magnet ratio (Fig. 7a). In line with results obtained in the non-calibration case, the active sensors clustered around the magnets implantation sites, over the distal and central area of the stump. Compared to previous results, more sensors were picked up

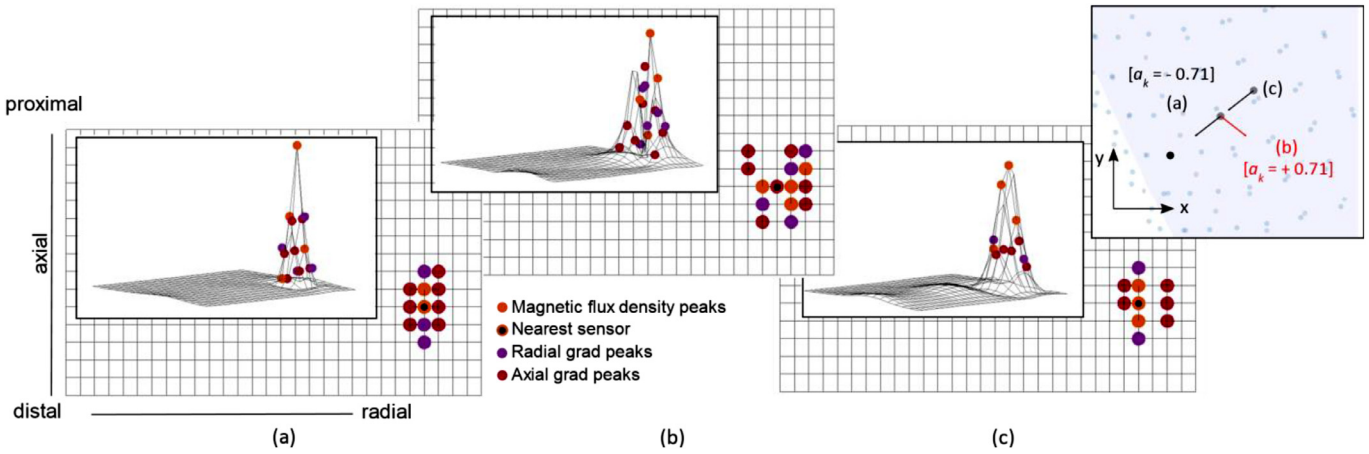

Fig. 4. Peaks generated by the magnet implanted in FCU when considering: the original implantation site (a), tilting of the x orientation component (inverted component sign) (b), and increased $L_{MM-sensor}$ by 10 mm, radially (c). The grids are the unfolded sensor array, where each vertex corresponds to a sensor. In (a), peaks distributed in a rectangular-like shape around the nearest sensor; in (b), the peaks narrowed towards the new pointing direction of the orientation vector, while widening on the opposite side; in (c), the peaks spread out, covering a larger area around the nearest sensor (a halved threshold for peaks was considered, to account for the increased $L_{MM-sensor}$). Three insets report the 3D view of the magnetic flux density in the three configurations. On the upper-right corner, the magnet positions (grey dots) and orientations (black (a)(c) and red (b) lines) are shown, with the black dot indicating the nearest sensor and the blue dots the other sensors.

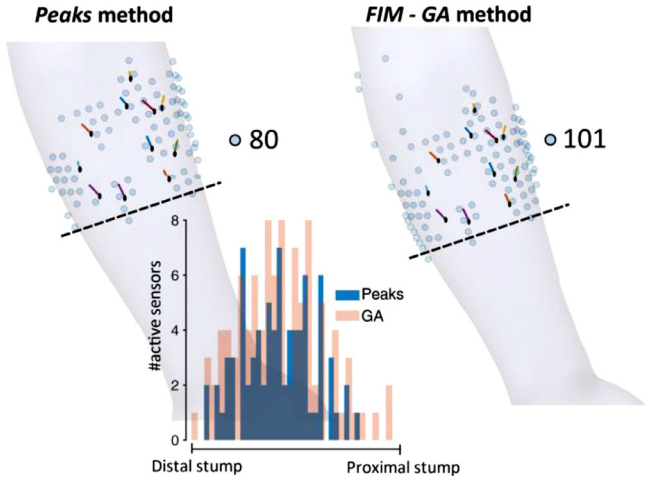

Fig. 5. Implanted magnets (black dots), associated trajectories (coloured segments), and active sensors (blue dots) derived through the *Peaks* (on the left) and the *FIM-GA* (on the right) method. The black dashed lines indicate the amputation level. The histograms show how the active sensors distributed across the stump in the two configurations.

around and along the magnets trajectories, while those more distant from the magnets rest position \ trajectory checkpoints were discarded (Fig. 7a).

An accurate localization in terms of both position and orientation was confirmed during muscles co-contraction (Fig. 7b-c). Indeed, a maximum E_p of 0.36 mm was obtained for the magnet implanted in FDS-I, whereas the one implanted in ED-II showed the highest E_o of 2.38°. Considering the shortest muscle displacement (ED-IV), the highest position error obtained for the corresponding magnet (0.19 mm) proved below 4% the total trajectory length. Regarding the smallest angular variation (FCR), the maximum orientation error for the corresponding magnet proved equal to 0.66°, thus below 9% the applied tilting. Again, error trends in term of position and orientation generally matched, as magnets which achieved higher E_p values also showed higher E_o values and vice-versa. In particular, the magnets implanted in ECRB, ED-II, ED-III and ED-IV compartments, as well as FDS-I showed higher median (position and orientation) errors compared to the other magnets (Fig. 7b-c).

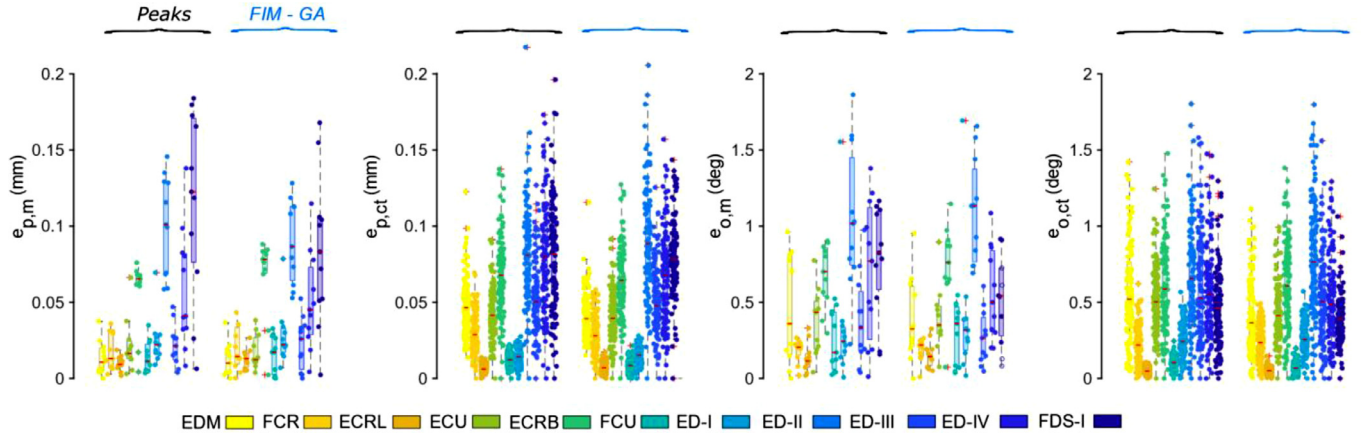

Fig. 6. Localization error in terms of position ($e_{p,m}$ and $e_{p,ct}$) and orientation ($e_{o,m}$ and $e_{o,ct}$) when using the active sensors selected with the *Peaks* and the *FIM-GA* method. Red crosses indicate the outliers, the boxplot encloses data within the interquartile range, the red line is the median value, whereas the whiskers extend to the limits of the distribution. Acronyms in Table I.

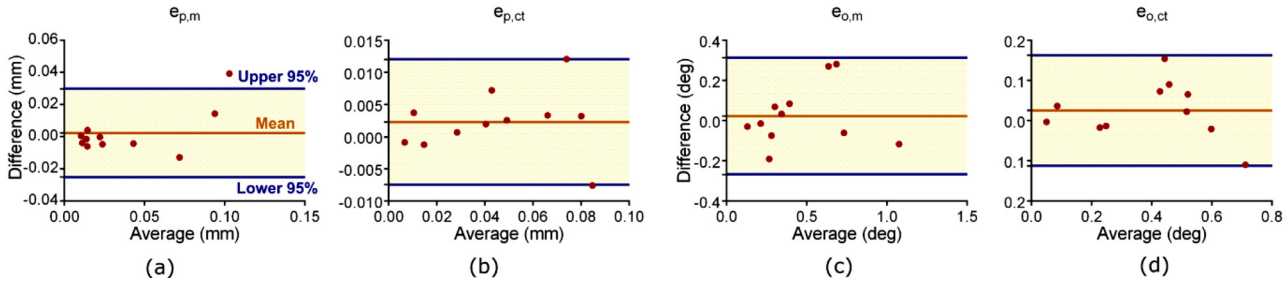

Fig. 7. Bland-Altman plots used to compare the localization accuracy obtained with the *Peaks* and the *FIM-GA* method. A plot was built for each of $e_{p,m}$ (a), $e_{p,ct}$ (b), $e_{o,m}$ (c) and $e_{o,ct}$ (d) pairs. Obtained data points always lied between the lower and upper limit of agreement expect for one point (a). The agreement between the two methods was confirmed.

4. Discussion

In this work, we assessed the validity of the *Peaks* method for identifying an optimal sensor set for a myokinetic control interface. We showed that the relevant information to select an optimal sensor set could be derived from the sensor readings and their spatial gradient, while no exact a-priori knowledge on the magnets position or displacement was needed. The localization achieved using the proposed method proved always accurate and statistically comparable to that obtained by applying methods adapted from the literature. As we indeed observed such performance, we conclude that the purpose of the study was fulfilled. In addition, we extended our approach by proposing a calibration phase aimed at customizing the sensor arrangement for a specific subject. To our knowledge, this is the first time that a sensor optimization algorithm is applied to multiple magnets while not being restricted to a planar configuration or specific application [8,12]. Nonetheless, these other approaches could be readily adapted/wrapped to the 3D case, e.g. by performing a transformation to curvilinear surfaces.

Outcomes from the single case study showed that the active sensor patterns changed according to the magnet orientation and implantation depth (Fig. 4), in a way closely resembling results from Talcoth and Rylander [9]. Notably, the change in the sensor pattern directly reflected that of the bell-shape waveform produced by the magnet on the field distribution (insets in Fig. 4), as already suggested in [14]. This further supports the idea that relevant information, like that identified analytically by minimizing the FIM, is related to the distinguishability and the topology of the peaks in the magnetic field (gradient). Indeed, both the minimization of the FIM and the *Peaks* method exploit the gradient of the magnetic field for selecting the sensors. The peaks of the gradients generally distribute around the magnetic marker, and this likely explains why in [9] sensors were selected around the transmitter and not directly above it. Indeed, the magnetic field absolute value is not involved in the FIM computation, vice versa its peaks are exploited here.

As the GA evolved some starting individuals through multiple iterations, the best solution reached when considering all magnets resembled that achieved by the *Peaks* method (Fig. 5). With both methods, the achieved position and orientation errors were always higher or comparable to the Bland-Altman plot limits of agreement, which proved below the tenth of a millimeter for the position and below 1° for the orientation (Figs. 6 and 7). Thus, as more than 95% of points lied within such limits (i.e., the difference between the paired measures proved always very low), we can conclude that the two methods led to comparable results. Nevertheless, unlike optimization procedures, the *Peaks* method led to such solution with no need of iterations (indeed, it is ∼15 faster) and no need of setting multiple parameters or constraints, except for the threshold value. In this regard, although defining an appropriate threshold required to evaluate the localizer performance, there was no need of knowing the exact magnets implantation site, which is instead required by the *FIM-GA* method. On one hand, the localizer was able to accurately retrieve the correct magnets poses even if we provided it with corrupted initial conditions, in line with results from related works [32]. At the same time, the muscle workspace (i.e. muscles belly) needed to assess the localizer performance could be made available by imaging techniques carried out before the implantation procedure. As an example, magnetic resonance examinations guarantee a ∼1 mm^3 spatial resolution, and could be useful for planning the surgical implantation. An accurate segmentation of muscles could be drawn from such acquisitions by applying proper post-processing techniques [33].

The muscle contraction model used in this study considered both axial and radial displacements, in accordance with actual deformations undergone by biological muscles during contraction. Interestingly, it was shown that a negative correlation exists between the muscle peak radial displacement and the muscle / tendon stiffness [24]. The latter is likely to decrease in individuals who experienced limb amputation, because of a reduced muscle activity which could lead to a condition known as disuse atrophy [34]. For this reason, it was of fundamental importance to assess the ability of the localizer in retrieving radial displacements with good accuracy, in view of the target application.

We argue that the higher localization errors achieved for the magnets in ECRB, ED-II and FDS-I (Fig. 6) are due to their specific implantation sites, in particular to their $L_{MM-sensor}$. Indeed, both the magnets in ECRB and ED-II were not implanted deeply enough to have their dimensions doubled, but had a $L_{MM-sensor}$ slightly below the required threshold (respectively equal to 13.9 mm and 14.8 mm). The same occurred to the magnets in ED-III and ED-IV ($L_{MM-sensor}$ equal to 14.9 mm) which in turn showed larger localization errors, especially for the calibration phase results (Fig. 8). Vice versa, FDS-I had its dimensions doubled, but was implanted in the deepest site ($L_{MM-sensor}$ of 25.8 mm). Notably, as extensively assessed in early works [14,15], the R value (i.e. the ratio between the minimum inter-magnets distance and $L_{MM-sensor}$) can be used to get a more thorough prediction of the expected localization accuracy. Indeed, we previously showed that lower R values lead to lower localization accuracies, because being near to other magnets negatively affects the accuracy besides localization depth. In this case, the geometrical arrangement of magnets resulted in a lower R value for those (listed above) that achieved lower localization accuracies, with a mean R value equal to 1.45, against a mean value of 2.14 for the remaining ones.

The co-contractions simulated in the calibration phase were just representative examples of possible real scenarios, in which likely the activation level would not be the same in all involved muscles (here, we considered the maximum displacement for all units). Nevertheless, we have no reason to think these results would not extend to other muscles (compartments) or to differ-

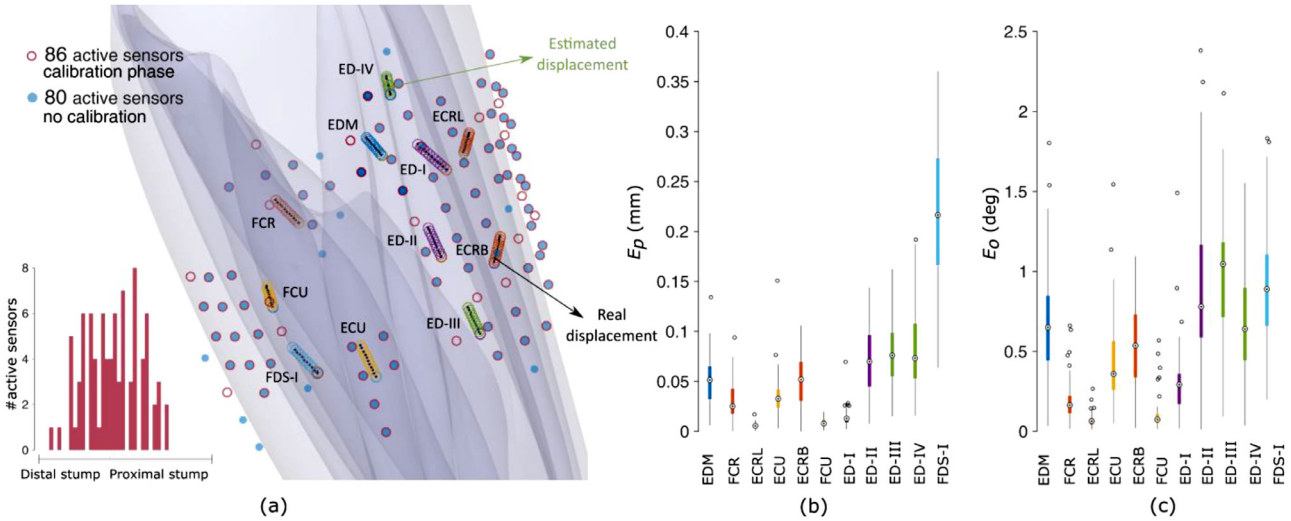

Fig. 8. Calibration phase results. (a) Actual and estimated magnet poses. Selected active sites without (blue dots) and with (empty red dots) calibration are displayed. The inset in the left-bottom corner reports the distribution of the active sites selected with the calibration phase over the stump. Localization errors in terms of position (b) and orientation (c) are shown in the boxplots. Boxes having the same colour indicate muscles that were contracted together. The empty dots indicate the outliers, the boxplot encloses data within the interquartile range, the dot is the median value, whereas the whiskers extend to the limits of the distribution. Acronyms in Table I.

ent activation levels. Notably, the feasibility of achieving accurate localization in the worst condition, that is when magnets are implanted in adjacent compartments (thus, particularly near to each other) was assessed here.

We observed that the threshold used for identifying peaks can be significantly increased by tuning the magnets dimensions and integrating information about muscle contraction. Increasing the threshold allows to improve the system robustness against the intrinsic sensor noise. Notably, the reduction of the critical value by 200 mG was chosen as a robust safety limit accounting for eventual electromagnetic noise sources [35]. On the other hand, the absolute final threshold value could vary across individuals, according to the magnets and sensors distribution in space allowed by specific anatomical conditions. The number of active sensors did not significantly increase following the calibration phase (from 80 to 86), and this supports the idea, previously suggested by Maréchal et al. [11], that optimizing the spatial arrangement is more important than increasing the number of sensors. This could possibly explain the lower sensor-to-magnet ratio obtained here (between 7.3 and 9.2) compared to results from the literature (between 8 and 15). Indeed, an improved spatial arrangement could allow to reduce the number of sensors needed for achieving the same accuracy. Not least, the calibration strategy proposed here could be easily re-applied to adapt to changes in muscle contractile properties following the user's training, thus providing an adaptive, customizable active sensor distribution.

The present study was indeed limited in some respects. First, although the muscle contraction model used in [15] was improved here by adding radial displacements and magnets tilting, it is still a simplification of the biological muscles complexity. Besides, assumptions made in [15] to standardize the maximum displacement and distal aponeurosis length across different muscles were maintained here. To make the contraction model more physiologically appropriate, differences across forearm muscle contractile properties, change in muscles conditions after the amputation surgery, and other relevant aspects should be considered. Despite this, here we proved the feasibility of accurately tracking position and orientation displacements during both independent and dependent activations. Thus, we hypothesize that localization would be accurate also in real conditions, as we can expect the displacement imposed by biological muscles to be a combination of those tested here. Furthermore, to our knowledge, no previous study investigated muscles displacement in depth, because current prostheses control strategies rely on electrical signals coming from the muscles and the nerves, and not on such data. Additional clinical investigations as well as more complex simulators would be needed to make the contraction model more realistic.

Secondly, the choice of setting $w = 0.5$ as threshold value for the sensor weights to be selected was arbitrary. Nevertheless, when inspecting the final weight vectors, we noticed that either a sensor was selected (i.e. $w \geq 0.5$) or its weight was equal (or really close to) zero, also because of the applied FIM normalization. Thus, no ambiguity in the final sensor selection was present. Notably, the choice of encoding the weights as real number instead of binary ones, which introduced the need of setting a threshold, allowed in turn to relax the constraint imposed to the weight sum, thus reducing the rigidity of the algorithm search.

4.1. Conclusions

We proved that the *Peaks* method is a viable, fast, and relatively simple approach for optimizing a sensing system design for multiple magnets tracking systems. It allows to achieve results comparable to those obtained with more complex methods and analytical models, while being based on a simple intuition: discriminable magnets will leave discriminable traces in the sensor recordings. Thanks to the calibration phase, it guarantees a smooth adaptation to different anatomical conditions, essential feature for our target application. Although only clinical trials will allow for a proper comparison with alternative advanced methods for prosthesis control [36–38], we advocate that the proposed approach would remarkably improve the effectiveness and efficiency of a myokinetic control interface. More in general, all systems and (bio)medical applications exploiting magnetic tracking will benefit from the outcomes of this study.

Conflict of Interest

All authors declare no conflict of interest.

Acknowledgement

This work was supported by the European Research Council through the bidirectional MyoKinetic implanted Interface for Natural Control of Artificial limbs (MYKI) Project under Grant ERC-2015-StG and Grant 679820.

References

[1] J. Malmivuo, R. Plonsey, Bioelectromagnetism: Principles and Applications of Bioelectric and Biomagnetic Fields, 2012, doi:10.1093/acprof:oso/9780195058239.001.0001.
[2] N. Sebkhi, N. Sahadat, S. Hersek, A. Bhavsar, S. Siahpoushan, M. Ghoovanloo, O.T. Inan, A Deep Neural Network-Based Permanent Magnet Localization for Tongue Tracking, IEEE Sens. J. (2019), doi:10.1109/JSEN.2019.2923585.
[3] V. Mack, D. Nißler, D. Kasikci, A. Malouhi, R. Aschenbach, U. Teichgräber, Magnetic Tracking and Electrocardiography-Guided Tip Confirmation System Versus Fluoroscopy for Placement of Peripherally Inserted Central Catheters: A Randomized, Noninferiority Comparison, Cardiovasc. Intervent. Radiol. (2020), doi:10.1007/s00270-020-02551-0.
[4] Z. Sun, L. Maréchal, S. Foong, Passive magnetic-based localization for precise untethered medical instrument tracking, Comput. Methods Programs Biomed. (2018), doi:10.1016/j.cmpb.2017.12.018.
[5] H.M. Shen, D. Ge, C. Lian, Y. Yue, Real-time passive magnetic localization based on restricted kinematic property for tongue-computer-interface, IEEE/ASME Int. Conf. Adv. Intell. Mechatronics, AIM, 2019, doi:10.1109/AIM.2019.8868405.
[6] S. Tarantino, F. Clemente, D. Barone, M. Controzzi, C. Cipriani, The myokinetic control interface: tracking implanted magnets as a means for prosthetic control, Sci. Rep. 7 (2017) 17149, doi:10.1038/s41598-017-17464-1.
[7] S. Tarantino, F. Clemente, A. De Simone, C. Cipriani, Feasibility of Tracking Multiple Implanted Magnets with a Myokinetic Control Interface: Simulation and Experimental Evidence Based on the Point Dipole Model, IEEE Trans. Biomed. Eng. (2020), doi:10.1109/TBME.2019.2935229.
[8] C. Hu, T. Ma, M.Q.H. Meng, Sensor arrangement optimization of magnetic localization and orientation cystem, IEEE ICIT 2007 - 2007, IEEE Int. Conf. Integr. Technol. (2007) 311–315, doi:10.1109/ICITECHNOLOGY.2007.4290485.
[9] O. Talcoth, T. Rylander, Optimization of sensor positions in magnetic tracking, 2011 Göteborg, Sweden.
[10] V. Schlageter, P.A. Besse, R.S. Popovic, P. Kucera, Tracking system with five degrees of freedom using a 2D-array of Hall sensors and a permanent magnet, Sensors Actuators, A Phys (2001), doi:10.1016/S0924-4247(01)00537-4.
[11] L. Maréchal, S. Foong, S. Ding, K.L. Wood, V. Patil, R. Gupta, Design optimization of a magnetic field-based localization device for enhanced ventriculostomy, J. Med. Devices, Trans. ASME. 10 (2016) 1–9, doi:10.1115/1.4032614.
[12] S. Song, X. Qiu, J. Wang, M.Q.H. Meng, Design and Optimization Strategy of Sensor Array Layout for Magnetic Localization System, IEEE Sens. J. (2017), doi:10.1109/JSEN.2017.2652470.
[13] M.S. Gibbs, G.C. Dandy, H.R. Maier, A genetic algorithm calibration method based on convergence due to genetic drift, Inf. Sci. (Ny). (2008), doi:10.1016/j.ins.2008.03.012.
[14] M. Gherardini, F. Clemente, S. Milici, C. Cipriani, Localization Accuracy of Multiple Magnets in a Myokinetic Control Interface, Submitt. to Sci. Rep. (2020).
[15] S. Milici, M. Gherardini, F. Clemente, F. Masiero, P. Sassu, C. Cipriani, The myokinetic control interface: how many magnets can be implanted in an amputated forearm? Evidence from a simulated environment, IEEE Trans. Neural Syst. Rehabil. Eng. (2020).
[16] S.L. Kilbreath, S.C. Gandevia, Limited independent flexion of the thumb and fingers in human subjects, J. Physiol. (1994), doi:10.1113/jphysiol.1994.sp020312.
[17] C. Cipriani, J.L. Segil, J.A. Birdwell, R.F. Weir, Dexterous control of a prosthetic hand using fine-wire intramuscular electrodes in targeted extrinsic muscles, IEEE Trans. Neural Syst. Rehabil. Eng. (2014), doi:10.1109/TNSRE.2014.2301234.
[18] G.N. Forman, D.A. Forman, E.J. Avila-Mireles, J. Zenzeri, M.W.R. Holmes, Investigating the Muscular and Kinematic Responses to Sudden Wrist Perturbations During a Dynamic Tracking Task, Sci. Rep. (2020), doi:10.1038/s41598-020-61117-9.
[19] C. Dai, H. Shin, B. Davis, X. Hu, Origins of Common Neural Inputs to Different Compartments of the Extensor Digitorum Communis Muscle, Sci. Rep. (2017), doi:10.1038/s41598-017-14555-x.
[20] G.M. Karst, Z. Hasan, Antagonist muscle activity during human forearm movements under varying kinematic and loading conditions, Exp. Brain Res. (1987), doi:10.1007/BF00248559.
[21] H. van Duinen, W.S. Yu, S.C. Gandevia, Limited ability to extend the digits of the human hand independently with extensor digitorum, J. Physiol. (2009), doi:10.1113/jphysiol.2009.177964.
[22] E.J. Rouse, D.C. Nahlik, M.A. Peshkin, T.A. Kuiken, Development of a model Osseo-Magnetic Link for intuitive rotational control of upper-limb prostheses, IEEE Trans. Neural Syst. Rehabil. Eng. 19 (2011) 213–220, doi:10.1109/TNSRE.2010.2102365.
[23] R.J. Baskin, P.J. Paolini, Volume change and pressure development in muscle during contraction, Am. J. Physiol. (1967), doi:10.1152/ajplegacy.1967.213.4.1025.
[24] L.J. Macgregor, A.M. Hunter, C. Orizio, M.M. Fairweather, M. Ditroilo, Assessment of Skeletal Muscle Contractile Properties by Radial Displacement: The Case for Tensiomyography, Sport. Med. (2018), doi:10.1007/s40279-018-0912-6.
[25] N. Derby, S. Olbert, Cylindrical magnets and ideal solenoids, Am. J. Phys. (2010), doi:10.1119/1.3256157.
[26] A. Caciagli, R.J. Baars, A.P. Philipse, B.W.M. Kuipers, Exact expression for the magnetic field of a finite cylinder with arbitrary uniform magnetization, J. Magn. Magn. Mater. (2018), doi:10.1016/j.jmmm.2018.02.003.
[27] A.E. Eiben, J.E. Smith, Natural Computing Series Introduction to Evolutionary Computing, 2015, doi:10.1007/978-3-662-44874-8.
[28] W. Yang, C. Hu, M. Li, M.Q.-H. Meng, S. Song, A new tracking system for three magnetic objectives, IEEE Trans. Magn. 46 (2010) 4023–4029, doi:10.1109/TMAG.2010.2076823.
[29] N. Gunantara, A review of multi-objective optimization: Methods and its applications, Cogent Eng 5 (2018) 1–16, doi:10.1080/23311916.2018.1502242.
[30] J.J. Moré, The Levenberg-Marquardt algorithm: Implementation and theory, 1978, doi:10.1007/bfb0067700.
[31] J.M. Bland, D.G. Altman, Measuring agreement in method comparison studies, Stat. Methods Med. Res. (1999), doi:10.1191/096228099673819272.
[32] J. Montero, M. Gherardini, F. Clemente, C. Cipriani, Comparison of online algorithms for the tracking of multiple magnetic targets in a myokinetic control interface, in: 2020, IEEE Int. Conf. Robot. Autom. (2020) Paris, doi:10.1109/icra40945.2020.9196804.
[33] C.M. Eng, S.R. Ward, L.H. Smallwood, G.D. Abrams, R.L. Lieber, Forearm muscle volumes can be accurately obtained from high resolution MRI, J. Biomech. (2006), doi:10.1016/s0021-9290(06)84732-9.
[34] B.A. Pascale, B.K. Potter, Residual Limb Complications and Management Strategies, Curr. Phys. Med. Rehabil. Reports. (2014), doi:10.1007/s40141-014-0063-0.
[35] V. Ianniciello, M. Gherardini, F. Clemente, C. Cipriani, Myokinetic prosthesis control oriented environmental magnetic disturb analysis, in: MEC20 Symp (2020).
[36] P.F. Pasquina, M. Evangelista, A.J. Carvalho, J. Lockhart, S. Griffin, G. Nanos, P. McKay, M. Hansen, D. Ipsen, J. Vandersea, J. Butkus, M. Miller, I. Murphy, D. Hankin, First-in-man demonstration of a fully implanted myoelectric sensors system to control an advanced electromechanical prosthetic hand, J. Neurosci. Methods. (2015), doi:10.1016/j.jneumeth.2014.07.016.
[37] T.A. Kuiken, G. Li, B.A. Lock, R.D. Lipschutz, L.A. Miller, K.A. Stubblefield, K.B. Englehart, Targeted muscle reinnervation for real-time myoelectric control of multifunction artificial arms, JAMA - J. Am. Med. Assoc. (2009), doi:10.1001/jama.2009.116.
[38] J.M. Hahne, M.A. Schweisfurth, M. Koppe, D. Farina, Simultaneous control of multiple functions of bionic hand prostheses: Performance and robustness in end users, Sci. Robot. (2018), doi:10.1126/scirobotics.aat3630.